

Nonconstant electronic density of states tunneling inversion for A15 superconductors: Nb₃Sn

J. K. Freericks, Amy Y. Liu, and A. Quandt

Department of Physics, Georgetown University, Washington, DC 20057-0995

J. Geerk

Forschungszentrum Karlsruhe, Institut für Festkörperphysik, P.O. Box 3640, D-76021 Karlsruhe, Germany

(Received 4 January 2002; published 31 May 2002)

We reexamine the tunneling data on A15 superconductors by performing a generalized McMillan-Rowell tunneling inversion that incorporates a nonconstant electronic density of states obtained from band-structure calculations. For Nb₃Sn, we find that the fit to the experimental data can be slightly improved by taking into account the sharp structure in the density of states, but it is likely that such an analysis alone is not enough to explain completely the superconducting tunneling characteristics of this material. Nevertheless, the extracted Eliashberg function displays a number of features expected to be present for the highest-quality Nb₃Sn samples.

DOI: 10.1103/PhysRevB.65.224510

PACS number(s): 74.70.Ad, 71.20.Be, 74.25.Jb, 74.25.Kc

I. INTRODUCTION

Twenty years ago, the A15 superconductors in the A₃B structure, with A a transition metal and B an *sp* metal, were the highest-transition-temperature superconductors known. The first such superconductor found was V₃Si, which was discovered¹ in the 1950s to have a T_c of about 17 K. In the ensuing years, other equilibrium compounds like V₃Ga and Nb₃Sn were discovered to have T_c 's in the range of 15–18 K. B-element-poor compounds like Nb₃Al, Nb₃Ga, Nb₃Ge, and Nb₃Si were also found, with T_c 's as high as 23 K. The structural, electronic, magnetic, elastic, vibrational, and superconducting properties of these materials were widely studied.^{2,3}

The use of tunneling spectroscopy to probe superconducting properties of the A15 materials was hindered by a number of materials issues. The fabrication of high-quality tunnel junctions was difficult because the use of native oxides for the tunneling barrier did not yield reproducible results, and hence artificial barrier layers had to be grown on top of the A15 superconductors.^{4,5} As the quality of the tunneling data improved, it became clear that these materials do not exhibit the simple behavior seen in conventional strong-coupling *s*-wave superconductors like Pb, Hg, and Nb. In particular, the reduced tunneling density of states displays a rapid over-swing⁶ followed by a sharp return to zero at energies near and above the maximum phonon energy. A revision of the McMillan-Rowell tunneling analysis⁷ by Arnold and Wolf⁸ allowed these data to be fit to high precision by assuming the presence of an additional normal-metal layer (characterized by a width and a scattering strength) between the superconductor and the insulating barrier. However, to fit the most recent experimental data⁵ within this proximity-effect-modified tunneling theory, one needs to assume that the width of the normal region approaches zero while its scattering strength becomes unusually large.

Alternatively, it has been suggested that the rapid over-swing in the high-energy regime in the tunneling density of states is related to the presence of sharp structures in the electronic density of states near the Fermi level.⁶ Band-

structure calculations⁹ show that the electronic density of states in these materials has peaks of width on the order of 100 meV near the Fermi energy. Such sharp structures require, at the very least, a reformulation of the Migdal-Eliashberg¹⁰ many-body analysis to include effects of a nonconstant electronic density of states^{11–13} within an energy range on the order of the maximal phonon energies of the material.

Other theories of superconductivity in A15 compounds go beyond simply generalizing the standard Migdal-Eliashberg theory to allow for energy dependence in the density of states. For example, Yu and Anderson¹⁴ examine what happens in an electron-phonon system that is coupled strongly enough to have the single-electron (polaronic) phase become unstable to bipolaronic (preformed pair) phases. Such systems display quite different behavior, but these theories have not been developed to the point where direct comparison to materials-specific tunneling conductances can be made.

Since the discovery of the high- T_c cuprates, work on the A15 compounds has virtually ceased—this despite the many fundamental questions about these materials that remain open. In this paper, we investigate whether high-quality tunneling data for the A15 materials can be understood within a conventional Migdal-Eliashberg framework generalized to include an energy-dependent electronic density of states. We perform this analysis and extract an experimentally fit Eliashberg function $\alpha^2F(\Omega)$ and Coulomb pseudopotential μ^* for Nb₃Sn, which has $T_c = 18$ K. Data from high-quality tunnel junctions grown on this material are available.⁵

In Sec. II, we derive the formalism needed to numerically perform the tunneling inversion including a nonconstant electronic density of states. This derivation and the computational algorithm are different from those developed previously in that an exact analytic continuation that properly treats the Coulomb pseudopotential and allows the calculations to be performed relative to the normal state is employed. In Sec. III, we present our numerical results for the tunneling inversion with both constant and nonconstant electronic densities of states. Conclusions are presented in Sec. IV.

II. FORMALISM

Our analysis begins with the calculation of the band structure and electronic density of states (DOS). Calculations are carried out using the VASP package,¹⁵ a plane-wave-based density-functional code using ultrasoft pseudopotentials.¹⁶ The electronic wave functions are expanded in plane waves up to a cutoff of 219 eV, and the electron-electron interaction is treated within the local density approximation (LDA) with the Ceperley-Alder exchange-correlation functional.¹⁷ The Brillouin zone is sampled on a Monkhorst-Pack mesh¹⁸ of at least $20 \times 20 \times 20$ points. We find the optimized crystal structure to be tetragonal, with a small distortion of the Nb sublattice.¹⁹ The peaks in the density of states near the Fermi level are very sensitive to this sublattice distortion.

In conventional Migdal-Eliashberg theory,¹⁰ the electronic density of states is chosen to be a constant (with an infinite “bandwidth”), and the energy cutoff of the theory is provided by the finite range of the Eliashberg function $\alpha^2 F(\Omega)$, which measures the ability of a phonon of energy Ω to scatter electrons on the Fermi surface. When performing the many-body theory calculations, one begins on the imaginary axis, where the Coulomb pseudopotential has a sharp cutoff,²⁰ and then performs an exact numerical analytic continuation²¹ to calculate real-axis properties. This technique allows for a proper treatment of the “soft” cutoff for the Coulomb pseudopotential on the real axis. In addition, because the superconducting and normal states appear more and more similar at high energies and because of the finite frequency cutoff (chosen to be $6\Omega_{\max}$ here), the self-energy begins to deviate from the exact result in the normal state as the energy increases. One can correct for this by performing the perturbative expansion relative to the normal state. In this case, one adds the exact normal-state self-energy minus the normal-state self-energy calculated with the energy cutoff used in the superconducting theory.²² Such a scheme was used when examining effects of vertex corrections²³ in Pb. When an energy-dependent electronic density of states is used, such a computational scheme becomes problematic because there is no longer an exact analytic expression for the normal-state self-energy. Furthermore, a choice must be made for the energy cutoff, because, assuming a bandwidth on the order of a few eV and a temperature on the order of 0.1 meV, the number of Matsubara frequencies required for an energy cutoff set by the bandwidth would be too large to perform calculations efficiently.

We adopt an alternative scheme here. We start by first calculating the normal-state self-energy at $T=0$. Since the Matsubara frequencies become a continuum at $T=0$, such a calculation can be performed simply by replacing the Matsubara summations by integrals along the imaginary axis, which are computed using conventional quadrature techniques. Next, we choose the energy cutoff to be the same as that used in the constant density of states calculations: namely, $6\Omega_{\max}$. We calculate the self-energy in the normal state at T (relative to the normal state at $T=0$) with the finite energy cutoff and then add the $T=0$ normal-state self-energy (with no cutoff) to the finite-temperature self-energy. Then we calculate the superconducting self-energy relative to the

normal state at T using the same cutoff. Finally, we add the full normal-state self-energy at T to get the superconducting self-energy.

Our many-body formalism on the imaginary axis follows most closely to Ref. 13. We use a Nambu-Gor’kov formalism and evaluate the self-consistent perturbation theory (using dressed phonons) in the Hartree-Fock approximation. (The Hartree term provides just a constant shift to the chemical potential and is ignored.) Perturbative calculations are performed for the normal state and the superconducting state. We begin our analysis in the normal state, where the resulting self-consistent equations are

$$\chi'_m = T \sum_n \lambda_{m-n} \times \int d\epsilon \frac{\rho(\epsilon)}{\rho(E_F)} \frac{\mu_N - \epsilon - \chi'_n}{\omega_n^2 Z_n'^2 + (\mu_N - \epsilon - \chi'_n)^2}, \quad (1)$$

$$Z'_m = 1 + \frac{T}{\omega_m} \sum_n \lambda_{m-n} \times \int d\epsilon \frac{\rho(\epsilon)}{\rho(E_F)} \frac{\omega_n Z_n'}{\omega_n^2 Z_n'^2 + (\mu_N - \epsilon - \chi'_n)^2}. \quad (2)$$

A prime indicates the normal-state perturbation theory, $i\omega_n = i\pi T(2n+1)$ is the fermionic Matsubara frequency, $\chi'_m = \chi'(i\omega_m) = \text{Re}\Sigma'(i\omega_m)$ is the real part of the normal-state self-energy, and $Z'_m = Z'(i\omega_m) = 1 - \text{Im}\Sigma'(i\omega_m)/\omega_m$ is the so-called renormalization function determined from the imaginary part of the normal-state self-energy. The symbols λ_{m-n} are the electron-phonon coupling strengths,

$$\lambda_{m-n} = \lambda(i\omega_m - i\omega_n) = \int_0^\infty d\Omega \alpha^2 F(\Omega) \frac{2\Omega}{\Omega^2 + (\omega_m - \omega_n)^2}, \quad (3)$$

and $\lambda = \lambda_0$. The function $\rho(\epsilon)$ is the electronic density of states as determined by the band-structure calculation, and $\rho(E_F)$ is the density of states at the $T=0$ chemical potential of the band-structure calculation (E_F). The chemical potential in the normal state is μ_N . In the limit as $T \rightarrow 0$, the number of Matsubara frequencies becomes an infinite continuum, and the summations can be replaced by integrals. We find

$$\chi'_0(i\omega) = \frac{1}{2\pi} \int d\omega' \lambda(i\omega - i\omega') \int d\epsilon \frac{\rho(\epsilon)}{\rho(E_F)} \times \frac{\mu_{N0} - \epsilon - \chi'_0(i\omega')}{\omega'^2 Z_0'^2(i\omega') + [\mu_{N0} - \epsilon - \chi'_0(i\omega')]^2}, \quad (4)$$

$$Z'_0(i\omega) = 1 + \frac{1}{2\pi\omega} \int d\omega' \lambda(i\omega - i\omega') \int d\epsilon \frac{\rho(\epsilon)}{\rho(E_F)} \\ \times \frac{\omega' Z'_0(i\omega')}{\omega'^2 Z_0'^2(i\omega') + [\mu_{N0} - \epsilon - \chi'_0(i\omega')]^2}, \quad (5)$$

with the subscript zero denoting that the results are at $T=0$. Evaluating these integrals with quadrature routines is much more efficient than calculating the Matsubara sums with a large energy cutoff at finite temperature.

Our strategy for determining the functions $\chi'_0(i\omega)$ and $Z'_0(i\omega)$ is to create a nonuniformly spaced grid on the imaginary axis (we use 336 points), with an upper cutoff many times the electronic bandwidth. The grid is constructed in the following fashion. The first grid point is chosen to lie at $i\omega_0=0$. Subsequent grid points are chosen by adding the new step size to the old grid point $i\omega_{j+1}=i\omega_j+i\delta_j$, with δ_j increasing by a factor of 1.1 with each step from its initial value $\delta_0=0.09$ meV [hence $\delta_j=0.09 \times (1.1)^j$]. We restrict $\delta_j < 400$ meV—if δ_j would be larger than 400 meV, we set it equal to 400 meV. The grid is reflected about $i\omega=0$ to construct the negative frequency axis. The integrals are then evaluated using a simple Riemann sum over the nonuniform grid. Once the functions χ'_0 and Z'_0 are known on the grid points, we linearly interpolate to evaluate them at any point on the imaginary axis.

We employ the $T=0$ normal-state solutions as an approximate solution for high frequency. This is included by first calculating the normal-state perturbation theory at finite temperature, using the same Matsubara frequency cutoff as used in the superconducting state $\omega_c = 6\Omega_{\max}$, and then adding the difference between the $T=0$ normal-state solution and the finite- T solution to the superconducting solution, as shown below. We solve the following self-consistent equations for the normal-state self-energy at temperature T :

$$\chi'_m = T \sum_{|\omega_n| < \omega_c} \lambda_{m-n} \int d\epsilon \frac{\rho(\epsilon)}{\rho(E_F)} \left[\frac{\mu_N - \epsilon - \chi'_n}{\omega_n^2 Z_n'^2 + (\mu_N - \epsilon - \chi'_n)^2} \right. \\ \left. - \frac{\mu_{N0} - \epsilon - \chi'_0(i\omega_n)}{\omega_n^2 Z_0'^2(i\omega_n) + [\mu_{N0} - \epsilon - \chi'_0(i\omega_n)]^2} \right] + \chi'_0(i\omega_m), \quad (6)$$

$$Z'_m = 1 + \frac{T}{\omega_m} \sum_{|\omega_n| < \omega_c} \lambda_{m-n} \int d\epsilon \frac{\rho(\epsilon)}{\rho(E_F)} \\ \times \left[\frac{\omega_n Z'_n}{\omega_n^2 Z_n'^2 + (\mu_N - \epsilon - \chi'_n)^2} \right. \\ \left. - \frac{\omega_n Z'_0(i\omega_n)}{\omega_n^2 Z_0'^2(i\omega_n) + (\mu_{N0} - \epsilon - \chi'_0)^2} \right] (i\omega_n) \\ + [Z'_0(i\omega_m) - 1]. \quad (7)$$

These equations would be exact if the summations over Matsubara frequencies for the $T=0$ quantities were replaced by

integrals. Since the normal-state self-energy does not depend too strongly on T for low temperature, this approximation is accurate for low T . Note that the chemical potential μ_N typically changes by about 1 meV (at $T=1.2$ K) from the zero-temperature value μ_{N0} (in the nonconstant density of states case).

The final set of equations we need is for the superconducting phase. The self-consistent equations are calculated “relative to the normal state” at T :

$$\chi_m = T \sum_{|\omega_n| \leq \omega_c} \lambda_{m-n} \int d\epsilon \frac{\rho(\epsilon)}{\rho(E_F)} \\ \times \left[\frac{\mu_S - \epsilon - \chi_n}{\omega_n^2 Z_n^2 + (\mu_S - \epsilon - \chi_n)^2 + \Delta_n^2 Z_n^2} \right. \\ \left. - \frac{\mu_N - \epsilon - \chi'_n}{\omega_n^2 Z_n'^2 + [\mu_N - \epsilon - \chi'_n]^2} \right] + \chi'_m, \quad (8)$$

$$Z_m = 1 + \frac{T}{\omega_m} \sum_{|\omega_n| \leq \omega_c} \lambda_{m-n} \int d\epsilon \frac{\rho(\epsilon)}{\rho(E_F)} \\ \times \left[\frac{\omega_n Z_n}{\omega_n^2 Z_n^2 + (\mu_S - \epsilon - \chi_n)^2 + \Delta_n^2 Z_n^2} \right. \\ \left. - \frac{\omega_n Z'_n}{\omega_n^2 Z_n'^2 + [\mu_N - \epsilon - \chi'_n]^2} \right] + [Z'_m - 1], \quad (9)$$

and

$$\Delta_m Z_m = T \sum_{|\omega_n| \leq \omega_c} (\lambda_{m-n} - \mu^*) \int d\epsilon \frac{\rho(\epsilon)}{\rho(E_F)} \\ \times \frac{\Delta_n Z_n}{\omega_n^2 Z_n^2 + (\mu_S - \epsilon - \chi_n)^2 + \Delta_n^2 Z_n^2}. \quad (10)$$

Here $\Delta_m = \Delta(i\omega_m) = \Sigma_{12}(i\omega_m)/Z_m$ is the superconducting gap determined from the off-diagonal self-energy, μ^* is the Coulomb pseudopotential, and μ_S is the chemical potential in the superconducting state. Note that we add and subtract the normal-state results at finite temperature in order to ensure that the Matsubara frequency summations converge rapidly ($\omega_c = 6\Omega_{\max}$ is the cutoff frequency; the high-frequency tails are already included in the normal-state self-energy). This procedure allows for a rapid computation of the many-body Green's functions when there is an energy-dependent electronic density of states. We only calculate the Green's functions at the Matsubara frequencies here.

The chemical potentials in the normal and superconducting states are determined by the requirement that the electron density be equal to the equilibrium density of electrons for the given band. Our first step is to find the $T=0$ Fermi level for the band-structure density of states, which satisfies

$$\rho_e = 2 \int_{-\infty}^{E_F} d\epsilon \rho(\epsilon), \quad (11)$$

with the factor of 2 coming from spin. In the normal state at $T=0$, we use the $T \rightarrow 0$ limit of the identity $\rho_e = 2T \sum_n G(i\omega_n)$ and Eq. (11) to produce the self-consistent equation for μ_{N0} :

$$2 \int_{\mu_{N0}}^{E_F} d\epsilon \rho(\epsilon) = \frac{1}{\pi} \int d\epsilon \rho(\epsilon) \times \int d\omega \left[\frac{1}{i\omega Z'_0(i\omega) + \mu_{N0} - \epsilon + \chi'_0(i\omega)} - \frac{1}{i\omega + \mu_{N0} - \epsilon} \right]. \quad (12)$$

The normal-state chemical potential at finite T (we use $T = 1.2$ K for the tunneling inversion) is found by comparison with the normal state at $T=0$: $0 = 2T \sum_n [G(i\omega_n) - G(i\omega_n)]_{T=0}$ (note the $T=0$ sum is an approximation to the continuum integral). Finally, for the superconducting state, we use the comparison of the normal-state filling with the superconducting-state filling to find μ_S :

$$0 = \frac{T}{\pi} \int d\epsilon \rho(\epsilon) \times \sum_{|\omega_m| < \omega_c} \left[\frac{\mu_S - \epsilon - \chi_m}{\omega_m^2 Z_m^2 + (\mu_S - \epsilon - \chi_m)^2 + \Delta_m^2 Z_m^2} - \frac{\mu_N - \epsilon + \chi'_m}{\omega_m^2 Z_m'^2 + (\mu_N - \epsilon + \chi'_m)^2} \right]. \quad (13)$$

The next step is to calculate the self-energy on the real axis using an exact analytic continuation technique.²¹ We begin with the normal state at $T=0$. The self-energy satisfies

$$\begin{aligned} \Sigma'_0(\omega + i\eta) &= \frac{1}{2\pi\rho(E_F)} \int_{-\infty}^{\infty} d\omega' \lambda(\omega - i\omega') \\ &\times \int d\epsilon \frac{\rho(\epsilon)}{i\omega' Z'_0(i\omega') + \mu_{N0} - \epsilon - \chi'_0(i\omega')} \\ &+ \frac{1}{\rho(E_F)} \int_0^{\omega} d\Omega \alpha^2 F(\Omega) \int d\epsilon \\ &\times \frac{\rho(\epsilon)}{(\omega - \Omega) Z'_0(\omega - \Omega) + \mu_{N0} - \epsilon - \chi'_0(\omega - \Omega) + i\eta}, \end{aligned} \quad (14)$$

where $\eta \rightarrow 0^+$. This is a self-consistent equation, because the second integral contains the self-energy on the real axis from the definitions

$$Z'_0(\omega) = 1 - \frac{\Sigma'_0(\omega + i\eta) - \Sigma_0'^*(-\omega + i\eta)}{2\omega} \quad (15)$$

and

$$\chi'_0(\omega) = \frac{\Sigma'_0(\omega + i\eta) + \Sigma_0'^*(-\omega + i\eta)}{2}, \quad (16)$$

where the * denotes complex conjugation. The term $\lambda(\omega - i\omega')$ is found from the spectral formula and the given Eliashberg function $\alpha^2 F(\Omega)$:

$$\lambda(\omega - i\omega') = - \int_{-\infty}^{\infty} d\Omega \frac{\alpha^2 F(\Omega)}{\omega - i\omega' - \Omega}. \quad (17)$$

Now we calculate the finite- T normal-state results relative to the $T=0$ calculation:

$$\begin{aligned} \Sigma'(\omega + i\eta) &= \frac{T}{\rho(E_F)} \sum_{|\omega_n| < \omega_c} \lambda(\omega - i\omega_n) \int d\epsilon \left[\frac{\rho(\epsilon)}{i\omega_n Z'_n + \mu_N - \epsilon - \chi'_n} - \frac{\rho(\epsilon)}{i\omega_n Z'_0(i\omega_n) + \mu_{N0} - \epsilon - \chi'_0(i\omega_n)} \right] \\ &+ \frac{1}{2\rho(E_F)} \int_{-\infty}^{\infty} d\Omega \alpha^2 F(\Omega) \left[\tanh\left(\frac{\omega - \Omega}{2T}\right) + \coth\left(\frac{\Omega}{2T}\right) \right] \int d\epsilon \rho(\epsilon) \\ &\times \left[\frac{1}{(\omega - \Omega) Z'(\omega - \Omega) + \mu_N - \epsilon - \chi'(\omega - \Omega) + i\eta} - \frac{1}{(\omega - \Omega) Z'_0(\omega - \Omega) + \mu_{N0} - \epsilon - \chi'_0(\omega - \Omega) + i\eta} \right] \\ &+ \Sigma'_0(\omega + i\eta), \end{aligned} \quad (18)$$

where the Z and χ functions on the real axis are determined from equations analogous to Eqs. (15) and (16).

For the superconducting state, calculations are performed relative to the normal state at T :

$$\begin{aligned}
\Sigma_{11}(\omega + i\eta) = & T \sum_{|\omega_n| < \omega_c} \lambda(\omega - i\omega_n) \int d\epsilon \rho(\epsilon) \left[\frac{i\omega_n Z_n + \mu_S - \chi_n}{\omega_n^2 Z_n^2 + (\mu_S - \epsilon - \chi_n)^2 + \Delta_n^2 Z_n^2} - \frac{i\omega_n Z'_n + \mu_N - \chi'_n}{\omega_n^2 Z_n'^2 + (\mu_N - \epsilon - \chi'_n)^2} \right] \\
& + \frac{1}{2\rho(E_F)} \int_{-\infty}^{\infty} d\Omega \alpha^2 F(\Omega) \left[\tanh\left(\frac{\omega - \Omega}{2T}\right) + \coth\left(\frac{\omega - \Omega}{2T}\right) \right] \int d\epsilon \rho(\epsilon) \\
& \times \left[\frac{(\omega - \Omega)Z(\omega - \Omega) + \mu_S - \epsilon - \chi(\omega - \Omega)}{(\omega - \Omega)^2 Z^2(\omega - \Omega) + [\mu_S - \epsilon - \chi(\omega - \Omega)]^2 + \Delta(\omega - \Omega)^2 Z(\omega - \Omega)^2} \right. \\
& \left. - \frac{(\omega - \Omega)Z'(\omega - \Omega) + \mu_N - \epsilon - \chi'(\omega - \Omega)}{(\omega - \Omega)^2 Z'^2(\omega - \Omega) + [\mu_N - \epsilon - \chi'(\omega - \Omega)]^2} \right] + \Sigma'(\omega + i\eta), \tag{19}
\end{aligned}$$

for the diagonal self-energy and

$$\begin{aligned}
\Sigma_{12}(\omega + i\eta) = & T \sum_{|\omega_n| < \omega_c} [\lambda(\omega - i\omega_n) - \mu^*] \int d\epsilon \rho(\epsilon) \frac{\Delta_n Z_n}{\omega_n^2 Z_n^2 + (\mu_S - \epsilon - \chi_n)^2 + \Delta_n^2 Z_n^2} \\
& + \frac{1}{2\rho(E_F)} \int_{-\infty}^{\infty} d\Omega \alpha^2 F(\Omega) \\
& \times \left[\tanh\left(\frac{\omega - \Omega}{2T}\right) + \coth\left(\frac{\omega - \Omega}{2T}\right) \right] \int d\epsilon \rho(\epsilon) \times \Delta(\omega - \Omega) Z(\omega - \Omega) / \{(\omega - \Omega)^2 Z^2 \\
& \times (\omega - \Omega) + [\mu_S - \epsilon - \chi(\omega - \Omega)]^2 + \Delta(\omega - \Omega)^2 Z(\omega - \Omega)^2\}, \tag{20}
\end{aligned}$$

for the off-diagonal self-energy.

The tunneling conductance satisfies

$$\frac{[dI/dV]_S}{[dI/dV]_N}(\omega) = \text{Re} \left[\frac{\omega}{\sqrt{\omega^2 - \Delta^2(\omega)}} \right]. \tag{21}$$

The reduced density of states (RDOS) is the ratio of the tunneling conductance to the BCS tunneling conductance minus one, which becomes

$$\text{RDOS}(\omega) = \text{Re} \left[\frac{\sqrt{\omega^2 - \Delta_0^2}}{\sqrt{\omega^2 - \Delta^2(\omega)}} \right] - 1, \tag{22}$$

where Δ_0 is the superconducting gap, defined as the solution to the equation $\text{Re}\Delta(\omega) = \omega$ (at $\omega = \Delta_0$).

To solve all of these self-consistent equations and to invert the tunneling conductance to get the Eliashberg function, we begin with the LDA band-structure electronic density of states as input. We take the band to consist of the states that contain nine electrons below the Fermi level and four electrons above, corresponding to approximately ± 0.8 eV about E_F . Hence the electron filling satisfies $\rho_e = 9$. Our first step (i) is to determine the band-structure Fermi level E_F at $T=0$ by solving Eq. (11). Then we take two initial guesses for μ_N . (ii) For each μ_N , we self-consistently solve for Eqs. (1) and (2) at $T=0$. Once those functions are known, (iii) we use a one-dimensional root finder to solve Eq. (12) to determine μ_N . The next step is to determine the superconducting chemical potential μ_S and the

Coulomb pseudopotential μ^* . We first choose a guess for μ^* . With μ^* fixed, we choose two initial guesses for μ_S and (iv) self-consistently solve Eqs. (8), (9), and (10). Once those functions are determined, (v) we use a one-dimensional root finder to solve Eq. (13) and find μ_S . (vi) Now the real-axis equations for both the normal state at $T=0$, Eqs. (15) and (16), and the normal and superconducting states at T , Eqs. (18), (19), and (20), are solved self-consistently. Once the gap function $\Delta(\omega)$ is known, we can find the superconducting gap Δ_0 . (vii) Steps (iv), (v), and (vi) are repeated for different values of μ^* until we find the particular value where $\Delta_0 = 3.15$ meV, which is the superconducting gap for Nb_3Sn at low temperature. If we knew the correct Eliashberg function, then steps (i)–(vii) would be all that we need to calculate the RDOS from Eq. (22). But we need to find the best fit $\alpha^2 F(\Omega)$ that is consistent with the experimental RDOS. To do this, we simply employ the McMillan-Rowell procedure for the tunneling inversion. We start with a guess for $\alpha^2 F$. (viii) Next we calculate the functional derivative of how changes in the Eliashberg function affect the RDOS. The functional derivative is found by adding a small-weight Gaussian to $\alpha^2 F(\Omega)$ centered at a given frequency Ω_0 , repeating steps (ii)–(vii) to determine the RDOS and calculating the functional derivative by taking the difference of the new RDOS with the RDOS for the original Eliashberg function. This step (viii) is repeated for each frequency in the discrete $\alpha^2 F$ to determine the functional derivative matrix. The next step (ix) is to choose the weights for adjusting $\alpha^2 F$ to fit the experimental RDOS better. Since the functional derivative

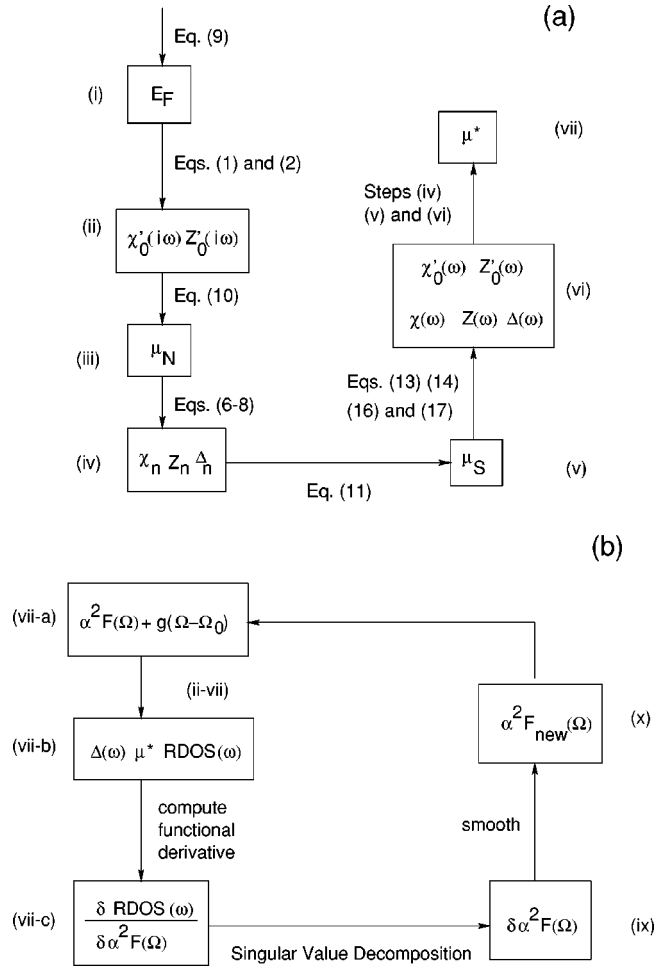


FIG. 1. Block diagrams of the algorithm employed in the modified McMillan-Rowell tunneling inversion with a nonconstant electronic density of states. In panel (a), we show the main algorithm used to determine the RDOS. Steps (i)–(vii) are described in detail in the text. Panel (b) shows the McMillan-Rowell strategy for updating the Eliashberg function in the tunneling inversion, with details described in the text.

matrix may be rank deficient, we use a singular-value decomposition to determine the updated weights. Once the updated $\alpha^2 F(\Omega)$ is found, (x) we apply an exploratory-data-analysis robust smoother followed by a Hanning smoother. Steps (viii)–(x) are repeated until the updated $\alpha^2 F(\Omega)$ ceases to produce a RDOS that is closer to experiment. We force the Eliashberg function to be positive everywhere and to be quadratic for $\Omega < 2.5$ meV. The step size for the discrete frequencies at which $\alpha^2 F$ is evaluated is 0.45 meV. The algorithm is depicted pictorially in Fig. 1.

There is a numerical problem with this algorithm. In general, the weights for the shift in $\alpha^2 F$ are strongly oscillatory, which forces the Eliashberg function to have large-amplitude narrow-width peaks. Since we do not expect the Eliashberg function to have such sharp peaks, they need to be smoothed away in the next update. Because the functional derivatives are not calculated with this smoothing procedure (and there is no obvious way to incorporate the smoothing into the de-

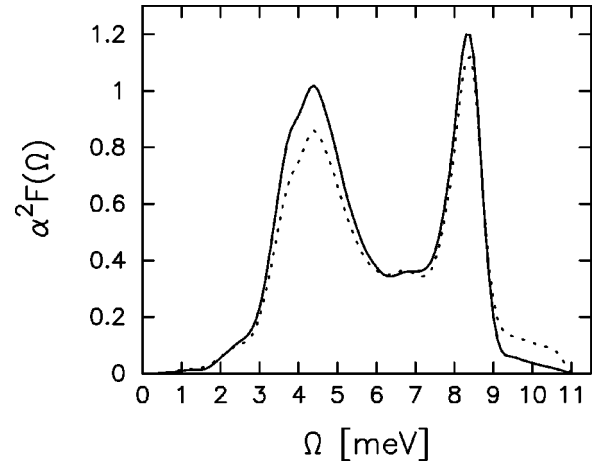


FIG. 2. Eliashberg functions for a tunneling inversion in lead with (solid line) constant density of states and (dotted lines) the nonconstant density of states of Nb_3Sn . The general shapes of the two curves are similar. The values of λ are 1.56 and 1.42 for the constant and nonconstant densities of states cases, respectively.

rivatives), we are limited as to how closely we can reproduce the experimental RDOS, even though we have the full freedom to adjust $\alpha^2 F$.

III. RESULTS

We first consider a test case, where the experimental tunneling data for lead is used to perform both a conventional and a nonconstant DOS tunneling inversion. In both cases we use the same code to perform the analysis as summarized in Fig. 1. In the constant DOS case, we use the DOS for lead (2.5×10^{-4} states per spin per meV per unit cell) and choose a band that contains two total electrons (including spin) and $\rho_e = 1$. In the nonconstant DOS case, we use the electronic DOS for Nb_3Sn (see inset to Fig. 5). This is of course an artificial problem that is presented for illustrative purposes.

The results for the best fit Eliashberg functions are given in Fig. 2. The solid line results from a tunneling inversion done with a constant DOS and is consistent with earlier analyses of the lead tunneling data ($\lambda = 1.56$, maximal error of 0.002, and a root-mean-square error of 0.0004). The tunneling-inversion result based on the energy-dependent Nb_3Sn DOS is plotted as a dotted line and corresponds to $\lambda = 1.42$, with a maximal error of 0.004 and a root-mean-square error of 0.0015. The fit with a nonconstant DOS is about 4 times worse than with the constant DOS. Note further that the main effect of the sharp peak in the DOS is to reduce the overall scale of $\alpha^2 F$ for nearly all frequencies except the highest, where it is strongly enhanced. Qualitatively, the two $\alpha^2 F$ curves are very similar in shape.

The quality of the tunneling data for lead is so good that one can actually see that the tunneling inversion works better with a constant DOS than with a nonconstant DOS. What is interesting is that one can get reasonable results using the wrong nonconstant DOS due to the freedom allowed in choosing the function $\alpha^2 F$.

We next turn to the results for the tunneling inversion of

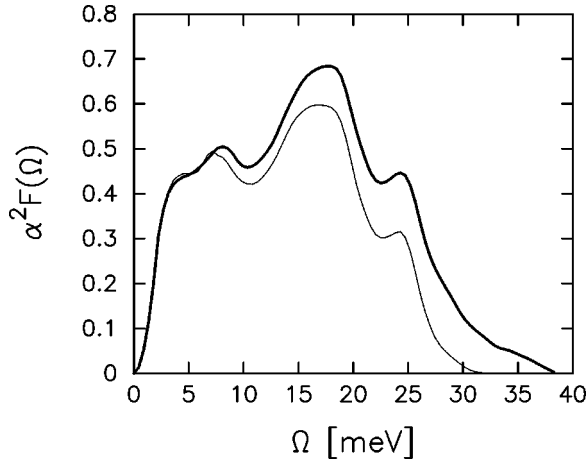


FIG. 3. Eliashberg functions for a tunneling inversion in Nb_3Sn for nonconstant density of states (thick line) and constant density of states (thin line). In the nonconstant density of states analysis, the spectral weight is enhanced at high energies.

Nb_3Sn . The extracted Eliashberg functions are shown in Fig. 3. The thick curve shows the nonconstant DOS results, while the thin curve is for the constant DOS case. The properties of these electron-phonon spectral functions are summarized in Table I. In contrast to the results for lead, where the Eliashberg function is reduced in the nonconstant DOS analysis, it is enhanced for Nb_3Sn . The main difference, aside from an overall scale factor, is a large enhancement for $\Omega > 20$ meV, particularly in the highest energies, where the constant DOS $\alpha^2 F$ is strongly suppressed. Note that the maximal allowed phonon frequency is the DFT-calculated 38 meV in both cases; the fitting procedure sharply suppresses the $\alpha^2 F$ at high energy for the constant DOS calculation. The general shapes of these curves are similar to those found previously⁵ but the overall scale is larger. The enhancement occurs because we are unable to reproduce the full overswing. In order to compensate for this, λ is increased and the quality of the low-energy fit is reduced. Note that we fit all experimental points, including those in the overswing region ($\omega > 35$ meV)—nevertheless, we are unable to get “good” results for the extracted $\alpha^2 F$ in the sense that the best fit $\alpha^2 F$ is unable to accurately reproduce the tunneling data over the entire experimentally measured range (due to the inability to produce the full overswing).

There are, nevertheless, a number of promising features of this calculation. If we compare Fig. 3 to the data for low- T_c (disordered) Nb_3Sn junctions, we find the broad low-energy peak and shoulder (present from 4 to 8 meV) lies a few meV lower in the high- T_c material than the low- T_c one⁵ (where it

TABLE I. Calculated properties of the Eliashberg function extracted from the tunneling inversion.

Inversion DOS	λ	μ^*	ω_{in} [meV]	A [meV]	T_c [K]	Error max.	Error rms
Nonconstant	2.738	0.286	7.072	13.652	19	0.033	0.0048
Constant	2.501	0.210	6.415	11.130	23	0.034	0.0055

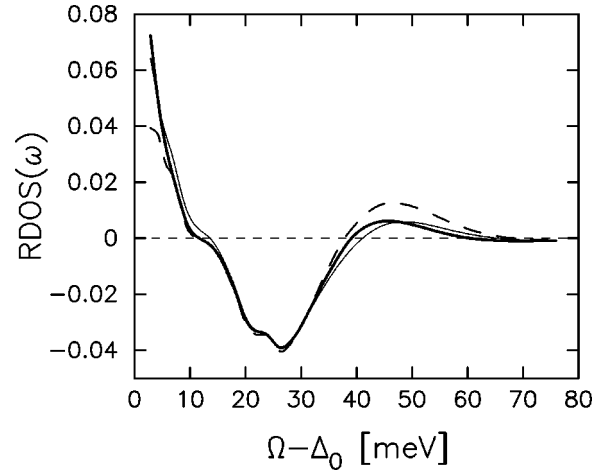


FIG. 4. Reduced density of states [from Eq. (22)] for nonconstant (thick) and constant (thin) density of states. The thick dashed line is the experimental data (scanned and digitized) and the thin dashed line is the horizontal axis. Note the poor quality of the fit at the lowest energies and the sharper overswing at high energies for the nonconstant density of states case. The poor fit arises from the fact that λ must be increased in order to produce the overswing, but this reduces the agreement at low frequencies. The results shown represent the best compromise for fitting the entire experimental spectrum.

lies at 10 meV). This is the expected phonon softening that leads to the high T_c of the A15 compounds that is evident also in second-derivative data²⁴ on Nb_3Sn , where the low- T_c material has a large peak at 10 meV which disperses to two peaks (one at 6 and one at 8 meV) in the high- T_c material. Another strong indication of enhanced electron-phonon coupling is the pronounced softening of the 10 meV shoulder observed in the phonon density of states of Nb_3Sn on cooling down from room temperature to 4.2 K as described by Schweiss *et al.*²⁵ Hence the extracted $\alpha^2 F$ displays the expected phonon-mode softening, with the expected energy scales. Another test is to compare the extracted $\alpha^2 F$ to the phonon DOS, $F(\Omega)$, measured with neutron scattering.²⁵ In actuality, neutron scattering weights the phonons by the neutron scattering cross section for each nucleus forming the generalized DOS $G(\Omega)$. Nb has a cross section approximately twice as big as Sn, but as the atomic masses of Nb and Sn are similar, we expect both atoms to be in motion for most phonon modes. Hence these modes can be excited by interactions of neutrons with either Nb or Sn nuclei. This averaging effect implies that the phonon density of states $F(\Omega)$ and the generalized density of states $G(\Omega)$ should agree closely^{25,26} for Nb_3Sn . If we take the ratio of the tunneling data to the neutron data, we find a large peak in $\alpha^2(\Omega)$ for energies below 10 meV. This agrees with theoretical calculations,²⁶ which predict a large $\alpha^2(\Omega)$ for the low-energy phonon modes (below 10 meV).

Next we consider the reduced density of states for both cases in Fig. 4. The thick dashed curve is the experimental data,⁵ the thin dashed line is the horizontal axis, the thick solid line is the nonconstant DOS case, and the thin solid line is the constant DOS results. There are three important points

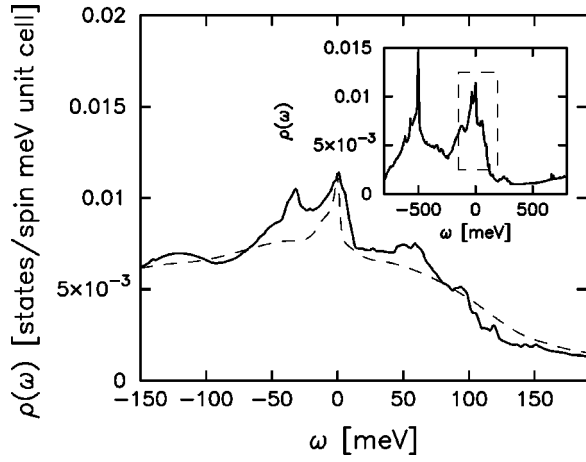


FIG. 5. Density of states for Nb₃Sn. The solid curve is the band-structure density of states as calculated with density-functional theory. The dashed curve is the quasiparticle density of states calculated with the fit α^2F . The chemical potential lies at $\omega = 0$. Inset shows the full band-structure density of states, with the dashed box indicating the region blown up in the main figure. The units of the vertical axis for both the main plot and the inset are states per spin per meV per unit cell.

to note about these curves: (i) the fits are poor at the lowest energies, (ii) the nonconstant density of states produces a more rapid “overswing” and return-to-zero at about 40 meV, and (iii) the amplitude of the overswing is enhanced in the region from 40 to 60 meV. As neither of the fits is particularly good, we cannot conclude from this work that the inclusion of nonconstant density of states effects alone is sufficient to explain the A15 tunneling data. But we do see that the incorporation of a nonconstant density of states definitely provides improvements. It is not clear what else is needed. Part of the problem may be with the numerical instabilities of the tunneling-inversion algorithm. Alternatively, there may be an intrinsic thin proximity layer that always needs to be taken into account regardless of the quality of the junction. Other factors that may be important include anharmonicity, anisotropy, and impurity scattering. It appears unlikely that disorder is the explanation, since disorder tends to reduce the magnitude of the RDOS, not increase it, as is needed. The proximity-effect explanation is also hard to support, because the constant DOS analysis found the proximity layer to be vanishingly thin. If that conclusion holds true for the nonconstant DOS analysis as well, then this would not be a viable explanation either. The effects of anharmonicity at low temperature should be explainable within a quasiharmonic approximation, unless there is a preformed-pair phase. Hence, we believe the most likely cause of the discrepancy is from anisotropic effects. It is conceivable that tunneling barriers grow differently on different indexed surfaces. The strong dependence of the tunneling conductance on barrier thickness thus could lead to a directional selectivity of the tunneling current and thereby anisotropy effects would influence the tunneling current even in the case of polycrystalline films. Incorporation of such anisotropic effects is beyond the scope of this work.

We conclude with a discussion of the properties of the

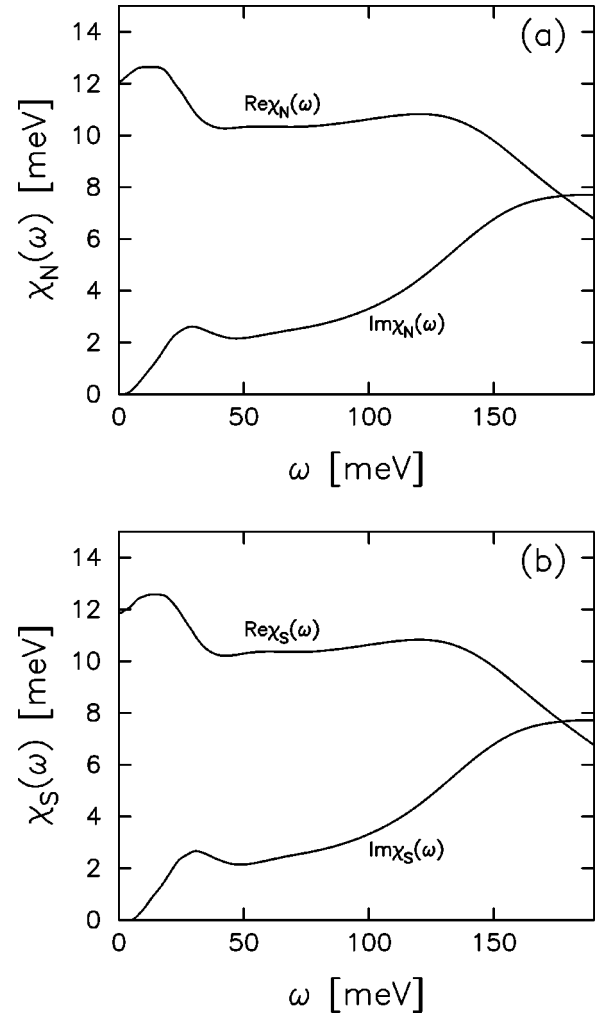


FIG. 6. Self-energy function $\chi(\omega)$ plotted in the (a) normal and (b) superconducting states. These functions are nearly identical, except for small differences at the lowest energies.

solutions to the many-body problem. The electronic density of states is shown in Fig. 5. The solid curve is the band-structure density of states as calculated within density-functional theory. The dashed curve is the quasiparticle density of states in the normal state at $T=0$ calculated with the fit α^2F . It depicts the behavior expected. The density of states is unchanged at the chemical potential ($\omega=0$) because the self-energy is momentum independent, the peak is narrowed by a factor of about 3 (due to “ $1+\lambda$ ” narrowing), and the overall density of states is smoothed out due to lifetime effects. In the inset, we show the full band-structure density of states used in the calculations. The dashed box indicates the region shown in the main figure.

In Fig. 6, we plot the real and imaginary parts of χ for (a) the normal state and (b) the superconducting state. This function vanishes for the case of a constant density of states. The chemical potentials are $\mu_N=15.70$ meV and $\mu_S = 15.97$ meV in the normal and superconducting states. The value of the real part of χ is of this order of magnitude. The normal and superconducting self-energies differ only at the lowest energies.

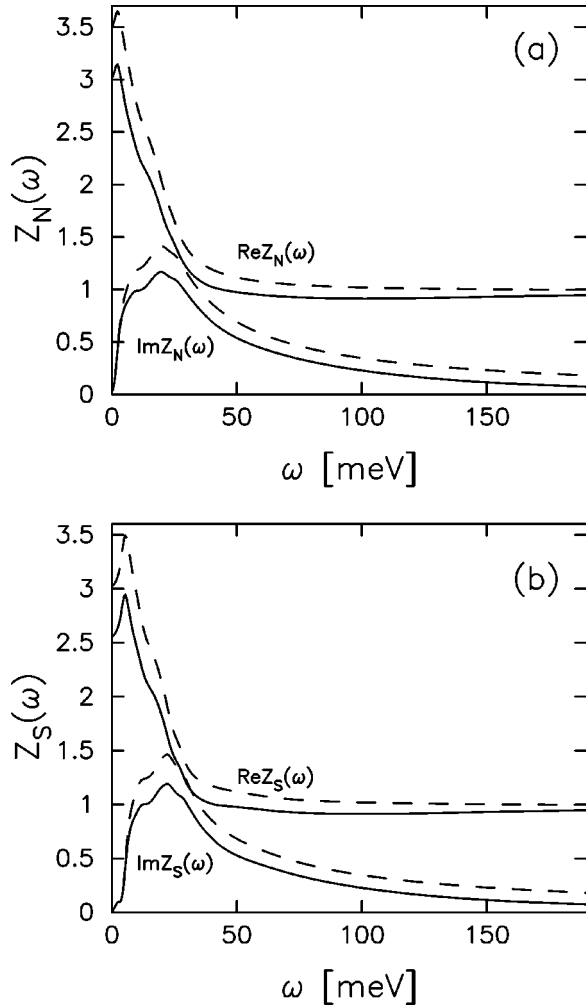


FIG. 7. The renormalization function for (a) the normal state and (b) the superconducting state. The solid curves are for a nonconstant density of states and the dashed curves are for a constant density of states. Note that $\text{Re}Z$ can dip below 1 for the nonconstant density of states case.

The renormalization function $Z(\omega)$ is plotted in Fig. 7 for (a) the normal phase and (b) the superconducting phase. The solid lines are for the nonconstant density of states case and the dashed lines are for the constant density of states case. Note how in the nonconstant density of states case, the effective strength of the electron phonon coupling, measured by $Z_N(0) - 1$, is closer to 2.1 than the value of λ , which is 2.7. It is the former value that is the true measure of the electron-phonon coupling strength with a nonconstant density of states. Note that the main differences between the nonconstant and constant densities of states calculations is that the overall scale is larger for the latter. These functions vary from the normal to the superconducting state only at low energies as expected. Note further that the real part of Z can dip below 1 for the nonconstant density of states case (it never does for a constant density of states).

Finally, the superconducting gap function $\Delta(\omega)$ is shown in Fig. 8. The results for the nonconstant density of states (solid line) and the constant density of states (dashed line)

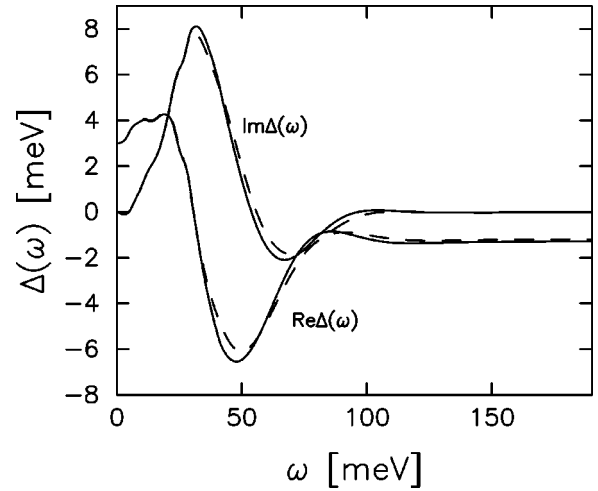


FIG. 8. Superconducting gap function for (solid) nonconstant density of states and (dashed) constant density of states. The two curves are nearly identical at low and high energies, but differ from about 30 meV to 130 meV. The sharp overswing in the experimental RDOS data is better reproduced by the more rapid formation of the high-energy peak (dip) in the real (imaginary) part of the nonconstant density of states gap function.

are nearly identical at both low and high energies. In the range from 30 meV to 130 meV, the curves deviate from each other: in the nonconstant density of states case, the peak (real part) and dip (imaginary part) form faster than in the constant density of states case. This is what produces the sharper overswing in the RDOS for the nonconstant density of states calculation.

IV. CONCLUSIONS

We have performed a modified McMillan-Rowell tunneling inversion including the effects of the nonconstant electronic density of states near the Fermi level for Nb_3Sn . The Eliashberg function that is found by this inversion has a larger value of λ than generally accepted for this material, but the effective value of λ derived from the renormalization function is more reasonable. Our extracted $\alpha^2F(\Omega)$ also has a number of expected features including large peaks at about 6 and 8 meV representing the soft phonon modes and a sharply peaked $\alpha^2(\Omega)$ below 10 meV which agrees with the theoretical predictions. Even taking into account the energy dependence of the density of states, we are unable to produce excellent fits of the tunneling data, though we can better reproduce the overswing observed at high frequencies. We believe the problem is partially numerical, as the tunneling inversion tries to force sharp spikes into α^2F , but the fit is still too poor at the lowest energies and in the overswing region to say that properly including the energy dependence of the density of states is enough to completely understand the tunneling data. It may be that the tunneling is modified by anisotropic effects, by a narrow proximity-coupled layer, or by other effects such as anharmonicity.

ACKNOWLEDGMENTS

We would like to acknowledge stimulating discussions with M. Beasley, J. Carbotte, B. Klein, B. Mitrović, E. Nicol,

and D. Rudman. We also want to thank D. Rudman for sharing his data with us. This work was supported by the National Science Foundation under Grant No. DMR-9973225.

-
- ¹G.F. Hardy and J.K. Hulm, *Phys. Rev.* **87**, 884 (1953).
²L.R. Testardi, *Rev. Mod. Phys.* **47**, 637 (1975); M. Weger and I. B. Goldberg, in *Solid State Physics: Advances in Research and Applications*, edited by H. Ehrenreich, R. Seitz, and D. Turnbull (Academic, New York, 1973), Vol. 28.
³L.Y.L. Shen, *Phys. Rev. Lett.* **29**, 1082 (1972); J. Kwo and T.H. Geballe, *Physica B* **B109&110**, 1665 (1982).
⁴D.A. Rudman and M.R. Beasley, *Phys. Rev. B* **30**, 2590 (1984); D.A. Rudman, F. Hellman, R.H. Hammond, and M.R. Beasley, *J. Appl. Phys.* **55**, 3544 (1984).
⁵J. Geerk, U. Schneider, W. Bangert, H. Rietschel, F. Gompf, M. Gurvitch, J. Remeika, and J.M. Rowell, *Physica B* **135**, 187 (1985); J. Geerk, U. Kaufmann, W. Bangert, and H. Rietschel, *Phys. Rev. B* **33**, 1621 (1986).
⁶B. Mitrović and J.P. Carbotte, *Physica B* **108**, 977 (1981); *Solid State Commun.* **40**, 249 (1981).
⁷W.L. McMillan and J.M. Rowell, *Phys. Rev. Lett.* **14**, 108 (1965); in *Superconductivity*, edited by R. Parks (Dekker, New York, 1969), Vol. 1, p. 117.
⁸G.B. Arnold, *Phys. Rev. B* **18**, 1076 (1978); G.B. Arnold, J. Zasadinski, J.W. Osmon, and E.L. Wolf, *J. Low Temp. Phys.* **40**, 225 (1980); E.L. Wolf, *Principles of Electron Tunneling Spectroscopy*, International Series of Monographs on Physics, Vol. 71 (Oxford University Press, New York, 1985).
⁹B.M. Klein, L.L. Boyer, D.A. Papaconstantopoulos, and L.F. Mattheiss, *Phys. Rev. B* **18**, 6411 (1978); K.M. Ho, M.L. Cohen, and W.E. Pickett, *Phys. Rev. Lett.* **41**, 815 (1978).
¹⁰A.B. Migdal, *Zh. Éksp. Teor. Fiz.* **34**, 1438 (1958) [*Sov. Phys. JETP* **7**, 999 (1959)]; G.M. Eliashberg, *ibid.* **38**, 966 (1960) [**11**, 696 (1960)].
¹¹G. Kieselmann and H. Rietschel, *J. Low Temp. Phys.* **46**, 28 (1982).
¹²W.E. Pickett, *Phys. Rev. B* **26**, 1186 (1982).
¹³B. Mitrović and J.P. Carbotte, *Can. J. Phys.* **61**, 758 (1983); **61**, 784 (1983).
¹⁴C.C. Yu and P.W. Anderson, *Phys. Rev. B* **29**, 6165 (1984).
¹⁵G. Kresse and J. Furthmüller, *Phys. Rev. B* **54**, 11 169 (1996); *Comput. Mater. Sci.* **6**, 15 (1996).
¹⁶D. Vanderbilt, *Phys. Rev. B* **41**, 7892 (1990); G. Kresse and J. Hafner, *J. Phys.: Condens. Matter* **6**, 8245 (1994).
¹⁷D.M. Ceperley and B.J. Alder, *Phys. Rev. Lett.* **45**, 566 (1980).
¹⁸H.J. Monkhorst and J.D. Pack, *Phys. Rev. B* **13**, 5188 (1976).
¹⁹Z.W. Lu and B.M. Klein, *Phys. Rev. Lett.* **79**, 1361 (1997); B. Sadigh and V. Ozolins, *Phys. Rev. B* **57**, 2793 (1998).
²⁰C.R. Leavens and E.W. Fenton, *Solid State Commun.* **33**, 597 (1980).
²¹F. Marsiglio, M. Schossmann, and J.P. Carbotte, *Phys. Rev. B* **37**, 4965 (1988).
²²F. Marsiglio (unpublished).
²³J.K. Freericks, E.J. Nicol, A.Y. Liu, and A.A. Quong, *Phys. Rev. B* **55**, 11 651 (1997).
²⁴U. Kaufmann, Ph.D. thesis, University of Karlsruhe, 1984; similar data for Nb₃Al appear in J. Geerk and W. Bangert, in *Proceedings of the 17th International Conference on Low Temperature Physics LT17*, edited by U. Eckern *et al.* (North-Holland, Amsterdam, 1984), p. 603.
²⁵L. Pintschovius, H.G. Smith, N. Wakabayashi, W. Reichardt, W. Weber, G.W. Webb, and Z. Fisk, *Phys. Rev. B* **28**, 5866 (1983); B.P. Schweiss, B. Renker, E. Schneider, and W. Reichardt, in *Superconductivity in d- and f-band Metals*, edited by D.H. Douglass (Plenum, New York, 1976), p. 189.
²⁶W. Weber, in *Electronic Structure of Complex Systems*, edited by P. Phariseau and W. Temmerman (Plenum, New York, 1984).